Turbulent Scalar Mixing in a Skewed Jet in Crossflow: Experiments and Modeling

Kevin J. Ryan[1] · Julien Bodart[2] · Mikko Folkersma[2] · Christopher J. Elkins[1] · John K. Eaton[1]

Abstract Turbulent mixing of an inclined, skewed jet injected into a crossflow is investigated using MRI-based experiments and a high-fidelity LES of the same configuration. The MRI technique provides three-dimensional fields of mean velocity and mean jet concentration. The 30° skew of the jet relative to the crossflow produces a single dominant vortex which introduces spanwise asymmetries to the velocity and concentration fields. The turbulent scalar transport of the skewed jet is investigated in further detail using the LES, which is validated against the experimental measurements. Mixing is found to be highly anisotropic throughout the jet region. Isotropic turbulent diffusivity and viscosity are used to calculate an optimal value of the turbulent Schmidt number, which varies widely over the jet region and lies mostly outside of the typically accepted range $0.7 \leq Sc_t \leq 0.9$. Finally, three common scalar flux models of increasing complexity are evaluated based on their ability to capture the anisotropy and predict the scalar concentration field of the present configuration. The higher order models are shown to better represent the turbulent scalar flux vector, leading to more accurate calculations of the concentration field. While more complex models are better able to capture the turbulent mixing, optimization of model constants is shown to significantly affect the results.

Keywords Jet in crossflow · Turbulent scalar flux · GDH · GGDH · HOGGDH · Modeling · Scalar transport

✉ Kevin J. Ryan
kjryan@stanford.edu

[1] Department of Mechanical Engineering, Stanford University, 488 Escondido Mall, Stanford, CA 94305, USA

[2] ISAE (Supaéro), Université de Toulouse, 10, avenue Edouard Belin, BP 54032 - 31055, Toulouse, CEDEX 4, France

1 Introduction

The jet in crossflow is a canonical problem in the study of fluid mechanics due to the complicated interaction of the jet, crossflow, and incoming boundary layer. The inclined and skewed jet in crossflow has found applications as vortex generating jets used for flow control and for film cooling of turbomachinery. The flow structure for this case has been examined in detail both experimentally [1, 2] and using highly resolved numerical models [3]. For film cooling applications, the primary interest is the ability to predict the mixing of the jet fluid, or coolant, with the mainstream. Large Eddy Simulation (LES) has been used to study turbulent mixing for unskewed film cooling jets [4, 5], however as shown by Johnson and Kapat [4] the results are not accurate unless very high grid resolution is used near the wall. Furthermore, Walters and Leylek [6] have shown that accurate simulations require a solution domain that also includes the jet supply plenum and the interior of the hole. Practically, this implies that LES studies are limited to simple configurations of a few jets at most. The computational cost of simulating flow around a turbine blade with numerous film cooling holes limits most design stage analysis to Reynolds-Averaged Navier-Stokes (RANS) calculations. In this framework, an additional model for the turbulent scalar fluxes is required to close the set of equations for the transport of the passive scalar.

Among existing scalar flux models, the most common is the Gradient Diffusion Hypothesis (GDH), which represents turbulent mixing as an augmented diffusion process by way of a turbulent diffusivity, α_t. While the turbulent diffusivity should rigorously be treated as a tensor, most implementations reduce the tensor to a spatially-varying scalar. The value of α_t is typically taken as ν_t / Sc_t, where the turbulent viscosity ν_t is available from the RANS momentum solution and turbulent Schmidt number is commonly set in the range $0.7 \leq Sc_t \leq 0.9$. This is the approach used for almost all practical film cooling computations (c.f. [3, 7]). This simplified form does not allow for anisotropy, as each component of the turbulent scalar flux is proportional to the corresponding component of the scalar concentration gradient. To allow for anisotropy between components, Daly and Harlow [8] proposed the Generalized Gradient Diffusion Hypothesis (GGDH). Abe and Suga [9] improved on the GGDH, which they found to underpredict the streamwise component in fully-developed turbulent channel flows, by introducing the Higher-Order Generalized Gradient Diffusion Hypothesis (HOGGDH). This latter formulation captures the correct scaling of the streamwise and wall-normal scalar flux components for flows with scalar concentration gradients primarily in the wall-normal direction.

Rossi and Iaccarino [10] implemented the GDH, GGDH, and HOGGDH models in a RANS calculation of a scalar released in the wake of a square obstacle and found increased agreement between the turbulent scalar fluxes with the GGDH and HOGGDH models. While the more complicated models did show an improvement, there were still differences between model predictions and experiment. Part of the error is attributable to the use of the RANS velocity field, which has its own model uncertainty. Ling et al. [11] analyzed the same three models for an unskewed jet in crossflow using a velocity field provided by a LES. They found that switching from the GDH to the GGDH or HOGGDH improved scalar concentration predictions, but that the tuning of model parameters had a more significant effect than the switch between different models. Li et al. [12] removed the specification of model parameters in the HOGGDH by scaling an isotropic GDH-like formulation of the turbulent scalar fluxes by a constant evaluated using the anisotropy of the momentum solution. They applied this model to a 30° inclined hole with various skew angles and found improvements over predictions by the Realizable $k - \epsilon$ model, but did not compare against a tuned or even standard implementation of the HOGGDH. Azzi and Lakehal [13] combined the

GGDH with various higher order anisotropic models for the Reynolds stresses. However, it is unclear if changes in the temperature field predictions are due to changes in the predicted flow structure or to the anisotropy of the scalar flux model. A significant problem in all of the model tests is the fact that there are no direct measurements of the turbulent scalar flux in any jet in crossflow configuration.

The present work is a combined experimental and numerical investigation of a skewed jet in crossflow in which experimental results are used to identify important regions of the jet and to validate a high-resolution LES for the identical geometry. The validated LES provides turbulence statistics not available from the time-averaged experimental data that are then used to directly test various scalar flux models. A similar approach was followed by Ivanova et al. [7] for a perpendicular jet in crossflow, who found that common assumptions about the turbulent Schmidt number were grossly in error. They felt that their results would have been more definitive if a well resolved direct numerical simulation (DNS) had been used. In the present case, the LES is performed with near-DNS resolution and experimentally validated against both mean velocity and scalar concentration measurements to lend additional confidence to the turbulence results. The specific objectives of this paper are to investigate the capabilities and assumptions which go into existing models for turbulent scalar transport, to evaluate if the performance of anisotropic models justifies the increased complexity, and to understand the reasons for model deviations in various regions of the flow. Additionally, this paper provides a high-resolution, three dimensional data set of velocity and concentration fields of a skewed jet in crossflow with a fully validated LES of the same configuration.

2 Experimental Methodology

2.1 Experimental apparatus and setup

Experiments are conducted in a closed-loop water channel. The main flow channel is shown in Fig. 1. The remainder of the flow loop includes a large reservoir, conventional pumps, valves, and flowmeters connected by flexible tubing. In the main flow channel, diffusers with grids, a honeycomb, and 2:1 area ratio contraction provide flow conditioning upstream of the test section to homogenize the inflow and reduce large scale secondary flows, see Fig. 1. The cross-section of the test section, shown schematically in Fig. 2, is 50 mm x 100 mm. A boundary layer trip 1 mm tall located 210 mm upstream ($X/D = -36.2$) of jet injection provides a turbulent boundary layer of height $\delta/D = 1.9$, measured at $X/D = -2$.

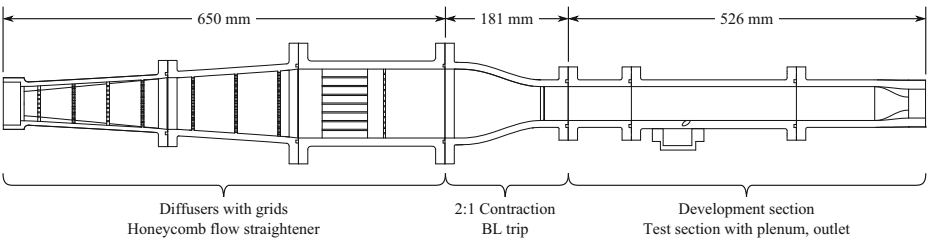

Fig. 1 Schematic of flow conditioning and test sections of the water channel. Flow is drawn from a reservoir to supply the crossflow inlet (*left*) and plenum inlet (beneath test section). Flow exiting the channel on the *right* is returned to the reservoir

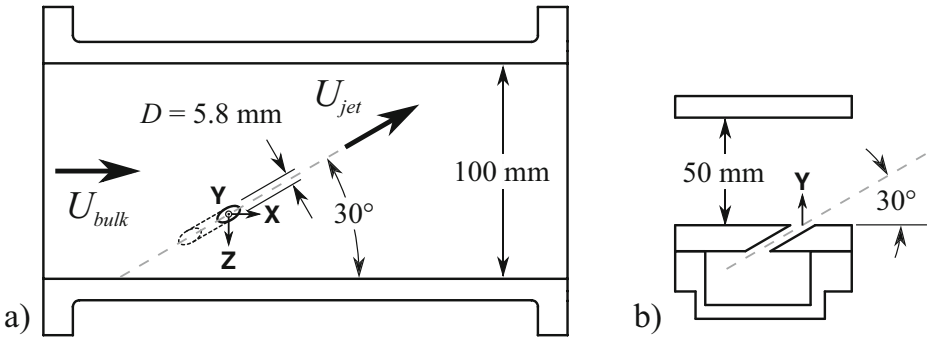

Fig. 2 Schematic of test section. **a** *Top view* of channel showing skew angle of jet. **b** Cross-section of channel viewed normal to jet hole symmetry plane. The jet feed plenum is visible below the channel. The origin of the coordinate system is the intersection of the jet hole axis with the *bottom* wall of the channel

The jet is injected from the bottom wall of the test section through a $D = 5.8$ mm diameter hole inclined 30° with respect to the wall, skewed 30° with respect to the crossflow in the channel, and $4.1D$ in length. The jet is fed from below by a plenum of size 40 mm x 25.4 mm x 34.8 mm. Flow to the jet plenum and main channel inlet are provided by separate pumps which draw from a common reservoir. The flowrates to the jet and crossflow are continuously monitored via paddlewheel flowmeters. This jet in crossflow configuration is operated at a blowing ratio of unity, with the bulk velocities of the crossflow U_{bulk} and jet U_{jet} maintained at 0.5 m/s. The resulting jet Reynolds number is $Re_D = 2900$. The jet geometry and operating conditions were chosen to be typical of discrete hole film cooling from the turbomachinery industry, c.f. McGovern and Leylek [3].

2.2 Magnetic resonance imaging (MRI) techniques

Three dimensional mean velocity and scalar concentration fields are acquired via magnetic resonance imaging techniques in two separate experiments. Magnetic Resonance Velocimetry (MRV) provides quantitative measurements of the flow velocity due to the sensitivity of the phase of the acquired signal to motion. Water is used as the working fluid, with copper sulfate added at a concentration of 0.06 M to enhance MRI signal magnitude. The procedure of obtaining three component velocity fields using MRV is detailed in Pelc et al. [14]. Thirteen individual scans, each lasting 9 minutes, are averaged to produce the final mean velocity field. The individual scans are performed in groups of 2 or 3, between which scans without flow ("flow-off") are collected. The flow-off scans are subtracted from the flow-on scans to remove the bias introduced by eddy currents in the MRI magnet.

The scalar field representing the concentration of jet fluid is measured using Magnetic Resonance Concentration (MRC), where the linear relationship between copper sulfate concentration and MRI signal magnitude is employed. The jet and crossflow are fed with different concentrations of copper sulfate; for the standard configuration the jet is fed with 0.0125 M and the crossflow is pure water. The inverse experiment, with copper sulfate in the crossflow and pure water in the jet, is also performed, and the two resulting fields are averaged to obtain the full 3D field of jet fluid concentration. Benson et al. [15] document the full procedure of data acquisition for MRC measurements. Twenty scans of each standard and inverted configuration, individually lasting 4.5 minutes, are averaged to increase the signal-to-noise ratio. The molecular Schmidt number for the diffusion of copper sulfate

in water is $Sc = 1500$. In the turbulent jet in crossflow, molecular diffusion is dominated by the turbulent transport and the effect of molecular diffusion on the spread of jet fluid can be considered negligible.

Both MRV and MRC experiments are performed using 3.0 Tesla GE full-body scanners at the Richard M. Lucas Center for Imaging at Stanford University. Data are acquired on a Cartesian grid measuring 0.66 mm x 0.6 mm x 0.6 mm in the streamwise, wall-normal, and spanwise directions, respectively, in a region beginning upstream of the jet and extending $20D$ downstream of injection. Measurements for MRV and MRC are acquired in Fourier space as spatial frequencies and reconstructed to 3D velocity and concentration fields. The resulting data are time-averaged over the acquisition length of the scan. Since the acquisition times for MRV and MRC are much longer than the time scales of turbulence and unsteadiness in the flow, the reconstructed fields accurately represent time-averaged quantities. Experimental uncertainty, calculated using an estimation of noise in the MRI signal and statistical variation of individual scans, is 4.3 % of U_{jet} for velocity components and 5.7 % for jet fluid concentration at 95 % confidence.

3 Numerical Setup

3.1 Large eddy simulation

The velocity and passive scalar concentration fields of the skewed jet in crossflow are also calculated with a high-fidelity LES using the finite-volume solver $CharLES^X$. The LES domain, shown in Fig. 3, uses the same geometry as the experiment and calculates the flow throughout the test section, including the jet hole supply plenum. The channel inlet in the simulation is located at $X/D = -40$, where a synthetic turbulent inflow is generated following the procedure used by Bodart et al. [16] for a similar flow configuration. The

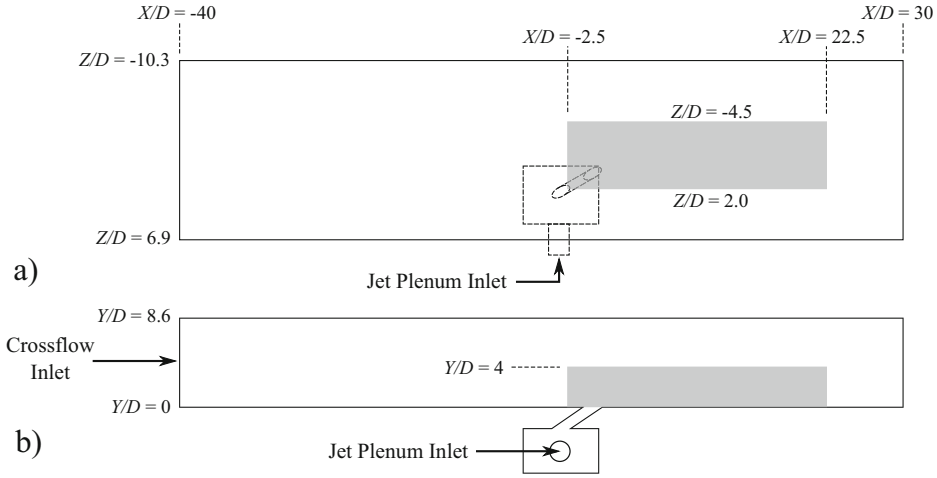

Fig. 3 **a** *Top* and (**b**) *side views* of the domain used for computations. The LES is performed on the region outlined in *black*, which extends from 40 hole diameters upstream of the jet hole to 30 hole diameters downstream in the streamwise direction, and includes the jet feed plenum. The *shaded region* is the domain of the RAST simulation, which is reduced in size from the LES domain to encompass only the region of jet interaction with the crossflow

distance between the LES inlet and jet injection is increased relative to the experiment to allow the synthetic turbulence to reach the correct physical behavior before interacting with the jet. A uniform inlet velocity is prescribed at the experimental inlet of the jet feed plenum, shown in Fig. 3. The experimental boundary layer trip is not included in the simulation, so turbulence is enforced by doubling the Reynolds numbers of the jet and channel flows, thus keeping the blowing ratio constant and recovering identical boundary layer profile and streamwise development characteristics upstream of the interaction.

The LES mesh contains a total of 101M cells, 17M of which are within the jet hole. Resolution is increased over the region of interaction of the jet and crossflow ($-1 < X/D < 10$, $0 < Y/D < 2$, $-2 < Z/D < 1$) to contain 18M cells with characteristic resolutions $\Delta X/D = 0.017$, $\Delta Y/D = 0.016$, and $\Delta Z/D = 0.019$. The viscous sublayer along the walls of the jet hole and bottom wall of the channel is fully resolved, with $y^+ < 1.5$. A molecular Schmidt number of $Sc = 1$ is used for transport of the passive scalar. Turbulence is expected to dominate scalar transport, so differences in molecular Sc between the experiment and LES are negligible. The filtered momentum equation is closed using the Vreman subgrid scale model [17], and the Reynolds analogy is used for the passive scalar with a fixed value of $Sc_{SGS} = 0.9$. Within the jet region, the SGS viscosity does not exceed 30 % of the molecular viscosity in most of the jet region, with a local peak near 50 %. The SGS model contribution can therefore be considered negligible.

LES convergence is examined by monitoring time-averaged streamwise velocity and turbulent kinetic energy along a streamwise profile within the jet at $Y/D = 0.6$, $Z/D = -0.6$. Time averages are computed from the LES during 252 time units ($T = D/U_{bulk}$), using 85,000 statistical samples. After 200 time units the monitored time averages remain unchanged within 1 % and 4 % for the streamwise velocity and turbulent kinetic energy, respectively, and the simulation is considered converged for first and second moment terms.

3.2 Reynolds-averaged scalar transport

In a separate framework, various turbulent scalar flux models are evaluated by solving the Reynolds-Averaged Scalar Transport (RAST) Eq. 1 for the jet fluid concentration field, $\overline{C}$. In the typical application of the RAST equation, the mean velocity $\overline{U_i}$ is obtained from RANS. The molecular diffusivity of the scalar, α, is a material property. To close the equation, a representation of the turbulent scalar flux, $\overline{u_i' c'}$, is required. Several common models for the turbulent scalar flux are presented and compared in Section 4.3. These models are built using components of the mean and fluctuating velocity, available from the RANS solution, leaving the mean concentration field $\overline{C}$ as the only unknown, which is then solved for.

$$\frac{\partial}{\partial x_i}\left(\overline{U_i}\,\overline{C}\right) = \frac{\partial}{\partial x_i}\left(\alpha \frac{\partial \overline{C}}{\partial x_i} - \overline{u_i' c'}\right) \tag{1}$$

The RAST simulations in this paper use the time-averaged velocity field provided by the LES for the advection of the scalar and evaluation of the turbulent scalar flux components in the RAST equation, and solve only for the scalar concentration field. As such, the mesh size and resolution is significantly reduced from the LES mesh. The mesh used for the RAST calculation spanned the jet region in the crossflow ($-2.5 \leq X/D \leq 22.5$, $0.0 \leq Y/D \leq 4.0$, $-4.5 \leq Z/D \leq 2.0$) and contains 3.4M hexahedral cells, concentrated at the bottom wall and near the exit of the jet hole. The location of the RAST domain relative to the LES domain is shown in Fig. 3. Calculations are performed in ANSYS Fluent using second-order upwinding for the advective fluxes. Turbulent scalar flux models are

implemented using user-defined functions (UDFs). The boundary conditions at the crossflow inlet ($X/D = -2.5$) and hole exit are constant values of jet fluid concentration at 0 and 1, respectively. The top, bottom, and spanwise sides of the domain are specified with adiabatic boundary conditions, and the downstream extent is set to an outflow condition. Calculations are considered converged when the residual of the scalar falls below 10^{-6}.

4 Results

Experimental results examining the features of the skewed jet in crossflow and turbulent scalar flux model evaluation are presented in the following sections. The X, Y, and Z coordinates denote streamwise, wall-normal, and spanwise coordinates (see Fig. 2) and are normalized by hole diameter D. Locations within the jet will be described as if viewed from upstream; "right" is in the positive spanwise direction, "left" is negative. Velocity components are normalized by jet bulk velocity U_{jet}, which is equal to the upstream freestream velocity in the crossflow. Jet fluid concentration $\overline{C}$ is normalized to be 0 and 1 at the inlets of the crossflow and jet, respectively.

4.1 Experimental results - jet features

The dominant feature of the jet in crossflow is a counter-rotating vortex pair (CVP) which develops inside the jet hole and governs much of the jet-crossflow interaction. The CVP lifts the jet off the wall and mixes crossflow fluid into the core of the jet. For the skewed jet configuration, one vortex of the pair quickly dissipates after injection, leaving a single vortex to control the development of the jet. Vorticity within the jet is visualized in Fig. 4 as contours of helicity, overlaid with in-plane mean velocity vectors. The second vortex is visible in the contour at $X/D = 4$, but this vortex quickly dissipates leaving a single vortex in the jet.

The effects of the vortex on the development of the jet are shown in Fig. 5, which has color contours of mean streamwise velocity and contour lines of jet concentration. The vortex carries low velocity fluid from the boundary layer beneath the jet up into the jet region. The vortex also entrains low concentration fluid from the crossflow into the jet region. The entrainment of slower, low concentration fluid occurs in the same location toward the left side of the jet, creating a distortion of the velocity and concentration contours. The rightmost extent of the $\overline{C} = 0.1$ contour remains at a spanwise position between $Z/D = 0.5$ and $Z/D = 0.6$ over several hole diameters of development. The left side of the jet, however, increases from a spanwise extent of $Z/D = -1.7$ to $Z/D = -2$ over the same distance. The preferential mixing at this one spanwise location has a clear effect on the lateral spread of jet fluid.

The jet concentration distribution is also linked to secondary flow features. The location of maximum jet concentration at each streamwise position correlates with the center of the jet vortex, located on the right side of the jet $-0.5 < Z/D < 0$. The asymmetry of the concentration maximum is another indication of different lateral mixing behavior. The spanwise location of the maximum concentration on each streamwise plane is plotted in Fig. 6a, along with the top view of the 3D isosurface of 10 % jet fluid concentration and the area-weighted spanwise center of the isosurface. For $X/D > 2.5$, the location of the maximum concentration is always at a greater spanwise value than the isosurface center, confirming the observations of Fig. 5. The spanwise variation in mixing behavior is important in the discussion of turbulent scalar flux models to follow. Similar behavior

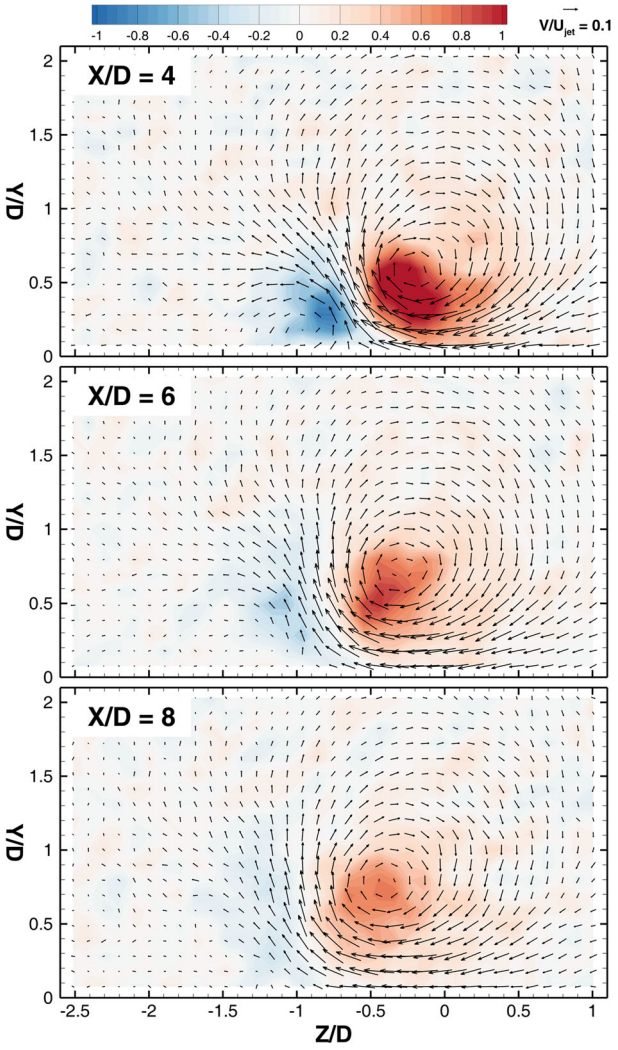

Fig. 4 Color contours of normalized helicity $\vec{\overline{U}} \cdot \vec{\overline{\omega}} / \left({U_{jet}}^2 / D \right)$ with vectors of in-plane mean velocity

is evident in Fig. 6b, where the presence of the wall inhibits mixing on the bottom of the jet. Again for $X/D > 2.5$, the isosurface center is consistently at a greater wall-normal coordinate than the concentration maximum. This indicates greater mixing toward the top of the jet as the isosurface penetrates further into the crossflow, while the highest concentration at a given streamwise location is located closer to the wall, where less mixing occurs.

4.2 Experimental validation of LES

The LES is validated by comparing contours of mean jet fluid concentration and mean velocity to the experimentally-determined fields. Detailed comparisons of the mean flow

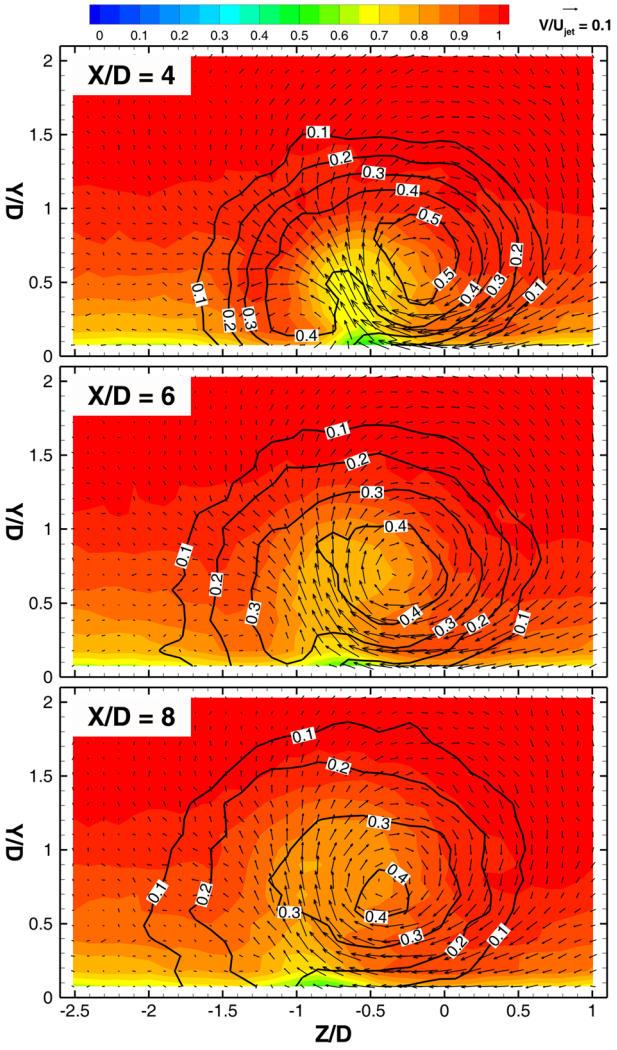

Fig. 5 Color contours of normalized mean streamwise velocity $\overline{U}/U_{jet}$ with vectors of in-plane mean velocity and contour lines of jet fluid concentration

features of the LES to the experiment show agreement to within experimental uncertainty. As examples, Fig. 7 shows comparisons of jet fluid concentration between MRC and the LES and Fig. 8 compares the streamwise velocity of the MRV and LES. The LES faithfully represents the mean velocity and concentration fields which lends confidence in the higher order moments extracted from the LES, $\overline{u_i' u_j'}$ and $\overline{u_i' c'}$.

4.3 Turbulent scalar flux modeling

The experimentally-validated LES is used to evaluate common turbulent scalar flux models. LES is an ideal tool for evaluating model performance due to the confidence in the Reynolds

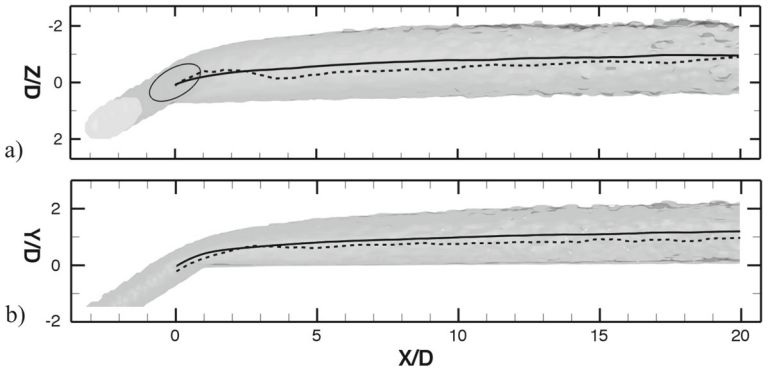

Fig. 6 **a** *Top* and (**b**) *side views* of 10 % jet fluid concentration isosurface. The *dashed line* is the locus of concentration maxima at different streamwise positions. The *solid line* is the area-averaged center of region enclosed by the isosurface. The *black ellipse* is the exit of the jet hole

stress tensor components, which must otherwise be modeled if RANS were used. With correct velocity fields from the LES, model form error can be decoupled from errors of using incorrect velocity fields to calculate turbulent scalar fluxes. Therefore, the error associated directly with the turbulent scalar flux model can be isolated from its inputs, and model

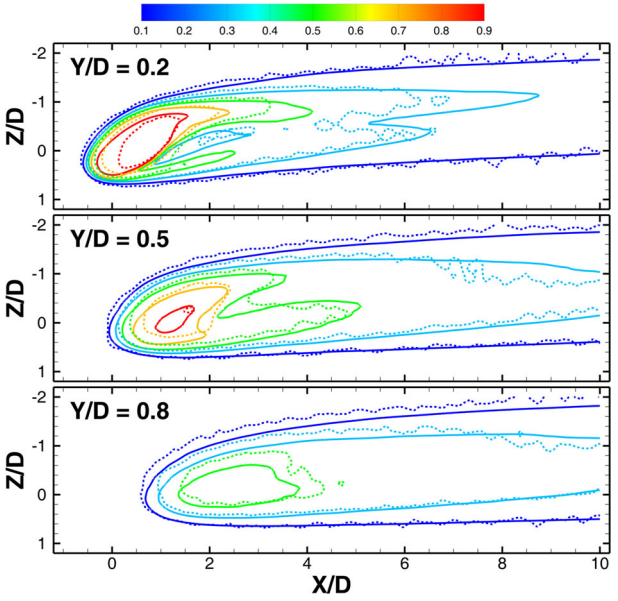

Fig. 7 Comparison of MRC (**- - -**) and LES (**—**) mean concentration on wall-normal planes. Concentration contours at 0.1, 0.3, 0.5, 0.7, and 0.9 are shown

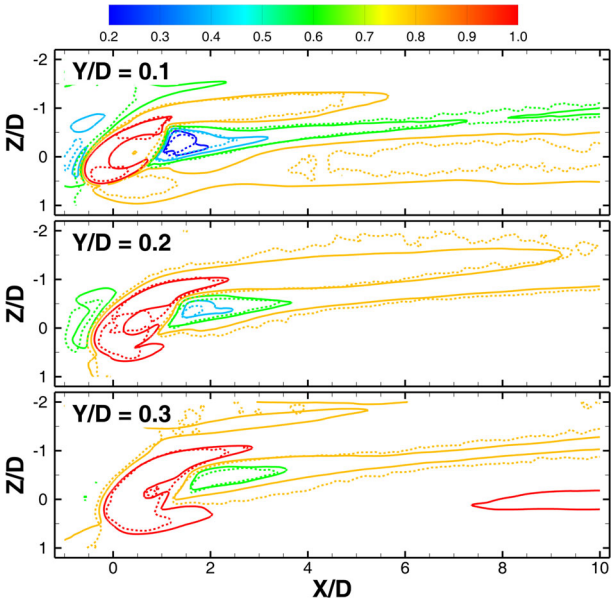

Fig. 8 Comparison of MRV (- - -) and LES (—) mean streamwise velocity on wall-normal planes. Velocity contours at 0.2, 0.4, 0.6, 0.8, and 1.0 U_{jet} are shown

performance can be evaluated directly. Three models are considered and compared: the GDH, GGDH, and HOGGDH.

$$\overline{u_i' c'}_{GDH} = -\alpha_t \frac{\partial \overline{C}}{\partial x_i} \tag{2}$$

$$\overline{u_i' c'}_{GGDH} = -\alpha_C \tau_C \overline{u_i' u_j'} \frac{\partial \overline{C}}{\partial x_j} \tag{3}$$

$$\overline{u_i' c'}_{HOGGDH} = -\alpha_C \tau_C \frac{\overline{u_i' u_k'}\,\overline{u_k' u_j'}}{k} \frac{\partial \overline{C}}{\partial x_j} \tag{4}$$

The GDH is defined by the turbulent diffusivity α_t, which in general is spatially-varying and anisotropic, but is commonly treated as isotropic and linked to the turbulent viscosity through the Reynolds Analogy, $Sc_t = \nu_t/\alpha_t$. The turbulent Schmidt number Sc_t is typically set at a constant value in the range $0.7 \leq Sc_t \leq 0.9$. The GGDH and HOGGDH are proportional to a turbulent time scale τ_C, typically taken as $\tau_C = k/\epsilon$, and model constant α_C.

4.3.1 Anisotropy

The GGDH and HOGGDH allow for increasingly more anisotropy over the standard GDH model. In its most general form the turbulent diffusivity is a tensor, through it can also be implemented as a vector, or most commonly, a scalar. To examine the anisotropy of the skewed jet in crossflow, the turbulent scalar fluxes $\overline{u_i' c'}$ and concentration gradient $\partial \overline{C}/\partial x_i$

extracted from the LES are used to calculate anisotropic components of the vector form of the turbulent diffusivity, $\alpha_{t,x}$, $\alpha_{t,y}$, and $\alpha_{t,z}$, as shown in Eq. 5.

$$\overline{u'c'} = -\alpha_{t,x}\frac{\partial \overline{C}}{\partial x} \qquad \overline{v'c'} = -\alpha_{t,y}\frac{\partial \overline{C}}{\partial y} \qquad \overline{w'c'} = -\alpha_{t,z}\frac{\partial \overline{C}}{\partial z} \tag{5}$$

These turbulent diffusivity components are shown in Fig. 9 at several streamwise locations within the jet region. Within each component, the value of turbulent diffusivity varies significantly over the jet region.

Low streamwise gradients of concentration artificially increase the value of $\alpha_{t,x}$, however the magnitude of the streamwise turbulent scalar flux $\overline{u'c'}$ remains small throughout the jet region and can be considered negligible compared to the mean convective flux $\overline{U}\,\overline{C}$. Therefore the discussion will focus on the wall-normal and spanwise components of the turbulent diffusivity. The $\alpha_{t,y}$ and $\alpha_{t,z}$ components in Fig. 9b and c show evidence of counter gradient diffusion, but these are limited to small regions where the mean concentration gradient goes to zero and thus does not represent a significant contribution to the overall scalar fluxes. What is more striking about these components is the asymmetry of the diffusivity magnitude on either side of the line denoting zero concentration gradient. The top half of the jet in Fig. 9b has an order of magnitude higher value of $\alpha_{t,y}$ than the bottom half of the jet, and the same trend holds for $\alpha_{t,z}$ for the left side of the jet over the right.

The ranges of $\alpha_{t,y}$ and $\alpha_{t,z}$ magnitudes are roughly the same over the jet region. The upper left region of the jet ($Z/D < 0$), where both $\alpha_{t,y}$ and $\alpha_{t,z}$ are positive and roughly the same magnitude, is a region where an isotropic turbulent diffusivity model would be

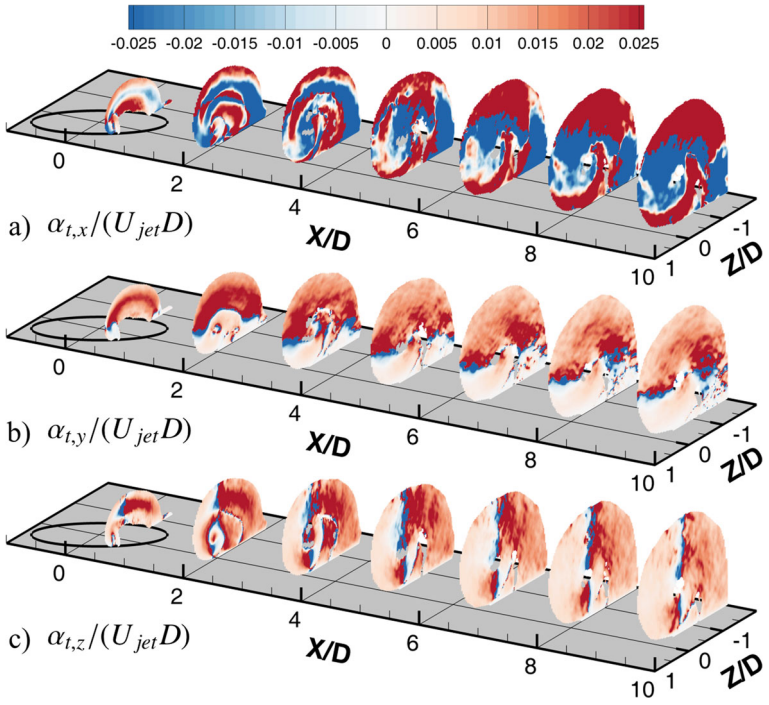

Fig. 9 Anisotropic components of turbulent diffusivity α_t. Streamwise slices of the jet region are blanked for $\overline{C} < 0.05$ for clarity, and for $D|\nabla\overline{C}| < 0.1$ where α_t is ill-defined. *Black ellipse* is the exit of the jet hole

accurate. However, this only represents a small portion of the jet region. Interestingly, this region is the same location where the preferential mixing shown in Fig. 5 occurs. Likewise, the intersection of the lines of zero concentration gradient corresponds with the location of maximum concentration of the jet and center of the jet vortex.

4.3.2 Isotropic values

Although Fig. 9 clearly invalidates the assumption of turbulent diffusivity isotropy, the isotropic GDH is still the most common turbulent scalar flux model employed. The LES can provide optimal isotropic, spatially-varying α_t and ν_t. These fields are used to test the assumption of a constant turbulent Schmidt number. Isotropic α_t and ν_t are found by weighting components of the turbulent scalar flux vector and Reynolds stress tensor by the mean concentration gradient $\partial\overline{C}/\partial x_i$ and mean strain rate tensor S_{ij}:

$$\alpha_t = -\overline{u_i' c'} \frac{\partial \overline{C}}{\partial x_i} \Bigg/ \frac{\partial \overline{C}}{\partial x_j} \frac{\partial \overline{C}}{\partial x_j} \tag{6}$$

$$\nu_t = -\overline{u_i' u_j'} S_{ij} \Big/ 2 S_{kl} S_{kl} \tag{7}$$

Isotropic values of α_t and ν_t along with turbulent Schmidt number Sc_t are shown in Fig. 10. Slices are blanked where the concentration gradient magnitude $D|\nabla C| < 0.1$, where α_t and Sc_t are ill-defined. The weighting of α_t and ν_t produces fields that are almost entirely positive, prohibiting the representation of any counter-gradient diffusion. The value of Sc_t varies drastically throughout the jet as seen in Fig. 10c, with most locations having $Sc_t < 0.5$ but smaller regions with $Sc_t > 1.5$. The region where $0.7 \leq Sc_t \leq 0.9$, represented in Fig. 10c by green-to-yellow contours, makes up only a small part of the jet with the largest region located near jet injection in the vicinity of the shear layer mixing above and below the jet.

4.3.3 Flux vector misalignment

The abilities of the GDH, GGDH, and HOGGDH to capture the anisotropy of the skewed jet in crossflow are evaluated by comparing the predicted turbulent scalar flux vectors given by Eqs. 2–4 to that extracted from the LES. The more common isotropic version of the GDH is used for this analysis. To remove any bias introduced by the choice of model constants α_C, turbulent diffusivity α_t, and turbulent time scale τ_C from the analysis, the angle ϕ between the turbulent scalar flux vectors of each models and that of the LES are compared. This metric is a more direct evaluation of model ability to capture flow anisotropy.

Figure 11 shows the misalignment angles for each of the three models considered, with angle reported in degrees. Data are blanked when $|\overline{u_i' c'}_{LES}| < 0.001$ where small deviations could produce large vector misalignment. The GDH shows significant misalignment throughout the jet region. Note that this implies that the scalar flux is not aligned with the concentration gradient. Only a small region has $\phi < 15°$, located mostly around the periphery of the jet, favoring the top and left sides. Two locations have near 90° misalignment: the first is near the bottom wall on the right side of the jet, the second is directly above this, near the location of maximum concentration identified in Fig. 5.

Figure 11b shows angle misalignment for the GGDH model. The anisotropy allowable by the GGDH has significantly reduced ϕ in much of the jet region. The left and top halves of the jet now show misalignment of 15° or less, and the first two slices shown feature large

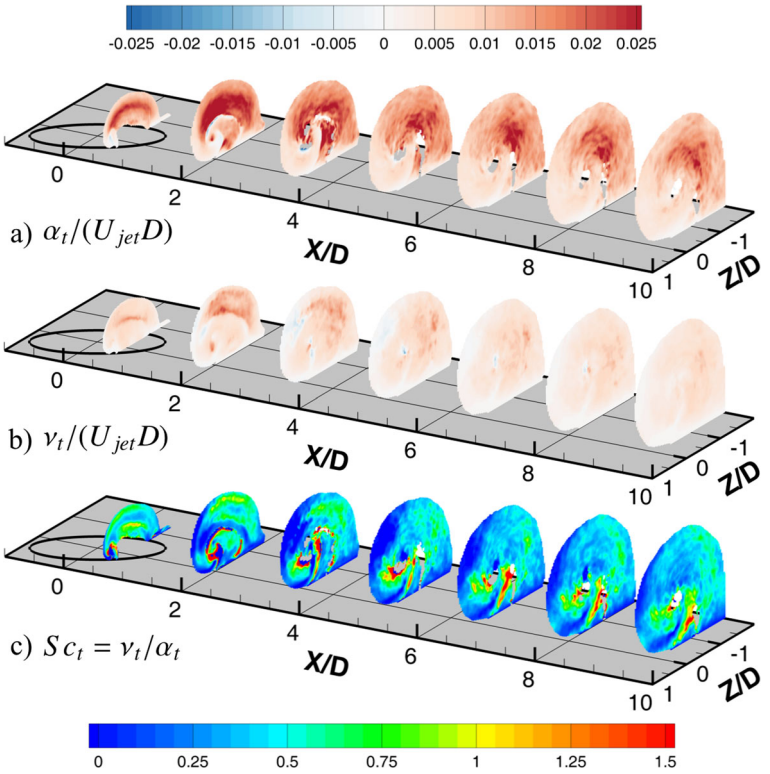

Fig. 10 Isotropic (**a**) turbulent diffusivity α_t, (**b**) turbulent viscosity ν_t, and (**c**) turbulent Schmidt number Sc_t. Streamwise slices of the jet region are blanked for $\overline{C} < 0.05$ for clarity, and for $D|\nabla\overline{C}| < 0.1$ where α_t and Sc_t are ill-defined. *Black ellipse* is the exit of the jet hole

regions of near-zero angle misalignment. Additionally, the near-wall region on the right side of the jet has been reduced by about 25°. The GGDH has worsened alignment in a few regions, one in particular being the middle of the right side of the jet. The region of $\phi > 60°$ has increased, and a larger area has an angle misalignment closer to 90°. The HOGGDH model makes some improvements over the GGDH, but also introduces angle misalignment in certain locations. The top and left halves of the jet are again well captured by the HOGGDH, with improvements of a few degrees over the GGDH. The most noticeable change occurs near the bottom wall on the right side of the jet. Although a thin layer of near 90° misalignment remains, the area directly above the wall has been reduced in large part below 15°. Misalignment increased in the same region as was observed with the GGDH, with a larger area near 90°.

4.3.4 Concentration field results

While the preceding analysis provides an indication of a model's best ability to capture anisotropy, the overall performance of the model when implemented will also depend on the choice of model constants. The three models discussed in Section 4.3.3 are used in the Reynolds-Averaged Scalar Transport (RAST) (Eq. 8) to calculate the jet fluid concentration

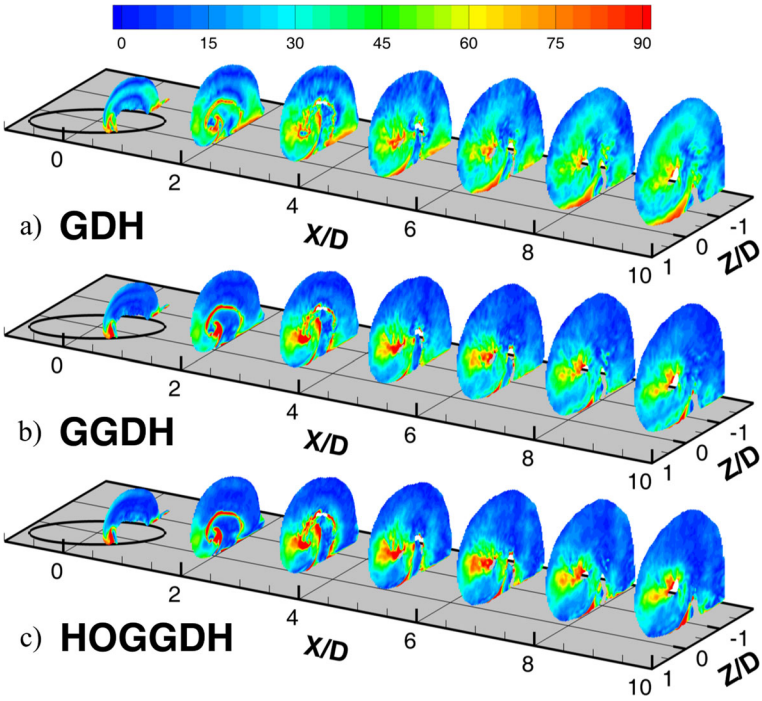

Fig. 11 Angle ϕ in degrees between turbulent scalar flux vectors $\overline{u_i' c'}_{LES}$ and $\overline{u_i' c'}_{Model}$ for (**a**) GDH, (**b**) GGDH, and (**c**) HOGGDH. *Black ellipse* is the exit of the jet hole

field. After the specification of a turbulent scalar flux model for $\overline{u_i' c'}$, this equation is solved for the only remaining unknown, the time-averaged concentration $\overline{C}$.

$$\frac{\partial}{\partial x_i}\left(\overline{U_i}\,\overline{C}\right) = \frac{\partial}{\partial x_i}\left(\alpha \frac{\partial \overline{C}}{\partial x_i} - \overline{u_i' c'}\right) \tag{8}$$

As is done with the analysis in Section 4.3.3, the LES solution is used to provide the required model inputs, with the exception of the mean concentration gradient $\partial \overline{C}/\partial x_j$ which was solved for in Eq. 8.

The dimensionless molecular diffusivity

$$\frac{\alpha}{U_{jet} D} = \frac{1}{Pe} = \frac{1}{Re\, Sc} \tag{9}$$

is specified at $\alpha/U_{jet}D = 1.724 \times 10^{-4}$ to match the Reynolds and molecular Schmidt numbers used in the LES calculation. For each of the three models introduced, multiple conditions are tested and their effect on the concentration field evaluated. Quantitative assessment of model performance is achieved by comparing the concentration field produced using the turbulent scalar flux model, $\overline{C}_{Model}$, to the time-averaged LES concentration field, $\overline{C}_{LES}$, using a scalar error metric based on the $L1$ norm of the difference between the concentration fields, Eq. 10.

$$E = \frac{\sum \left|\overline{C}_{LES} - \overline{C}_{Model}\right| w}{\sum w} \tag{10}$$

To reduce the influence of the large number of near-zero concentration cells in the domain, the summation in Eq. 10 is performed over the volume where $\overline{C}_{LES} > 0.001$. Summation is additionally restricted to the near-injection region, $X/D \leq 10$. The LES concentration field is interpolated onto the RAST mesh for this thresholding and for the computation of error E. The weighting function w is the cell volume of the RAST mesh.

For the GDH model, three different specifications of the turbulent diffusivity α_t are investigated. The first uses the optimal isotropic value of α_t (see Eq. 6 and Fig. 10a). To allow for convergence, the value of α_t is forced to be non-negative. As shown in Fig. 10a, this correction only effects a small portion of the domain. The remaining two cases use the GDH with the Reynolds Analogy (GDH-RA) by specifying $\alpha_t = \nu_t / Sc_t$, where ν_t is the isotropic turbulent viscosity (Eq. 7, Fig. 10b) and Sc_t is a prescribed value of the turbulent Schmidt number that is uniform over the flow field. Negative values of ν_t are truncated for convergence. Two values of Sc_t are tested: the default value of $Sc_t = 0.85$ commonly used in the GDH-RA formulation, and an optimized value of Sc_t which minimizes the error E.

Two specifications each are used for the GGDH and HOGGDH models, the first using the standard values of model constant α_C suggested by the literature: GGDH, $\alpha_C = 0.30$ [8]; HOGGDH, $\alpha_C = 0.60$ [9]. An optimized value of α_C is also found for each model following the procedure used to optimize Sc_t. Both GGDH and HOGGDH require the specification of time scale τ_C, normally taken as k/ϵ in a RANS solution. Since the dissipation rate ϵ is unavailable from the LES solution, the time scale is taken as

$$\tau_C = \frac{1}{\sqrt{S_{ij} S_{ij}}} \tag{11}$$

A summary of the seven model configurations including the evaluation of the error E is shown in Table 1.

Color contours of jet fluid concentration for the seven calculated configurations are shown in Fig. 12. The concentration field from the LES, interpolated onto the RAST mesh, is reproduced for comparison purposes.

As is evident from the evaluation of the error metric shown in Table 1 and in comparing the color contours of Fig. 12, the GDH model using the isotropic value of the turbulent diffusivity best captures the concentration field produced by the LES. This, however, is not surprising. This model uses the most information from the LES, and is the only one to use values from the scalar transport solution, including the correct values of the turbulent scalar fluxes and mean concentration gradient. The only simplifications used for this model are that α_t is made isotropic and restricted to be non-negative. As such, this model is not

Table 1 Summary of RAST calculations

Case	Model	Condition	$E \times 10^2$
1	GDH	$\alpha_t = \alpha_{t,iso}$	1.22
2	GDH-RA	$Sc_t = 0.85$	4.43
3		$Sc_t = 0.35$	2.10
4	GGDH	$\alpha_C = 0.30$	2.69
5		$\alpha_C = 0.45$	1.61
6	HOGGDH	$\alpha_C = 0.60$	1.77
7		$\alpha_C = 0.50$	1.69

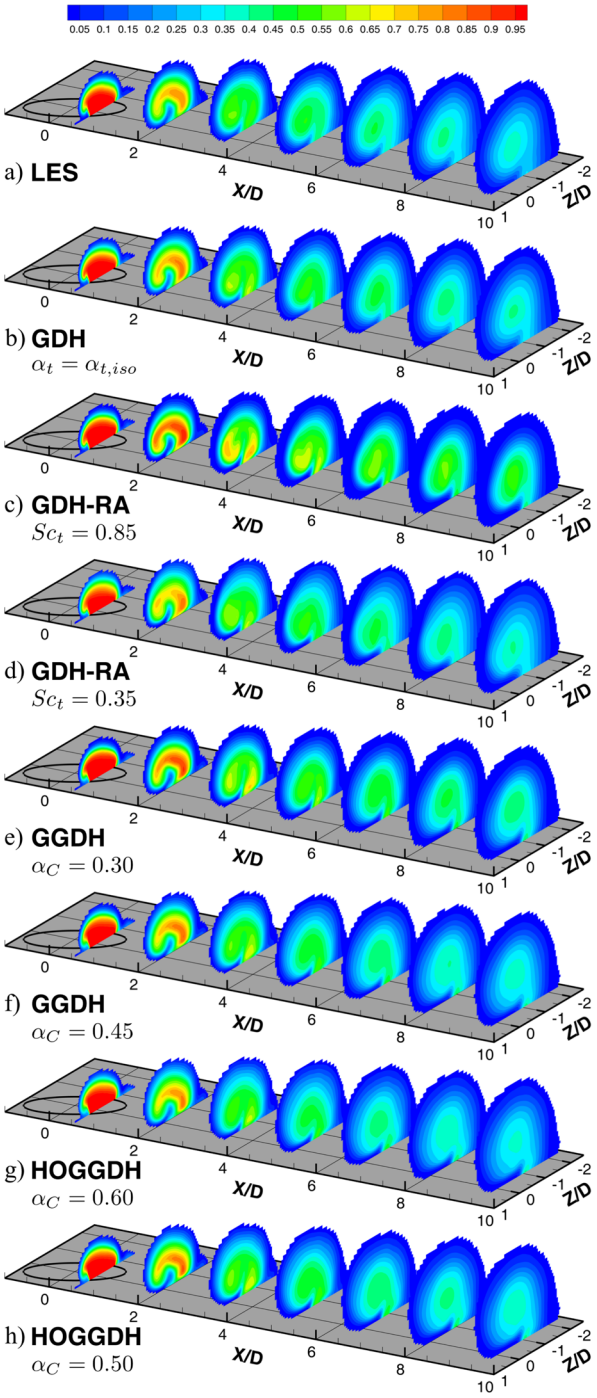

Fig. 12 Color contours of jet fluid concentration $\overline{C}$ from (**a**) LES and (**b–h**) RAST calculation using turbulent scalar flux models. Models are evaluated using both standard model constants (**c**, **e**, **g**) and optimized values (**d**, **f**, **h**). Contours are blanked where $\overline{C}_{LES} < 0.01$

useful for *a priori* calculation of the concentration field, but instead serves as a meaningful baseline for comparing the remaining models tested.

The GDH with the Reynolds Analogy still produces an isotropic model for the turbulent diffusivity, but only requires information from the momentum solution to evaluate. As shown in Fig. 12c, the GDH-RA model with the default turbulent Schmidt number $Sc_t = 0.85$ underpredicts the turbulent mixing in the jet, with higher values of jet fluid concentration and less spreading compared to the LES field. The error metric for this case is nearly 4 times that for Case 1. When the turbulent Schmidt number was changed to the optimized value $Sc_t = 0.35$, the scalar field more closely resembles the LES field in the magnitude and spread of jet fluid concentration, although there are still regions where the mixing has been over- and underpredicted, primarily in the first contours after injection and near the bottom wall. The error metric for the optimized Sc_t reduced by more than half of the Case 2 value, but is still nearly double the baseline isotropic value from Case 1.

The anisotropy allowed by the GGDH and HOGGDH models improve the predictions of the scalar concentration field, even when using the default values of α_C. Optimizing the model constants reduces the errors by roughly 40 % and 5 % for the GGDH and HOGGDH, respectively, and produces approximately the same error E. It should be noted that the improvement due to model constant optimization would also be influenced by the particular choice of time scale τ_C. The optimized anisotropic Cases 5 and 7 improve on the optimized isotropic Case 3 by more than 20 %, as was predicted in Fig. 11 with the improved representation of the turbulent scalar flux vector with the GGDH and HOGGDH models.

While Cases 5 and 7 perform well in the core of the jet region, there are significant differences between the modeled and LES concentration fields in the near-wall region. The jet concentration at the wall is shown in Fig. 13 for the LES, Case 1, and the three optimized cases (Cases 3, 5, and 7). All cases show higher concentration near the bottom wall than the LES. There are two regions where significant difference between the LES and modeled cases is evident: the upstream side of the jet hole exit and the bottom boundary of jet fluid concentration starting from $X/D = 2$ and extending downstream. At the upstream portion of the hole exit, every model predicts a higher concentration along the bottom wall than is seen in the LES, suggesting that the models predict a greater spanwise component of the turbulent diffusivity, drawing concentration from the jet exit along the wall in the spanwise direction. At the downstream region, the opposite problem occurs. The models predict weaker turbulent scalar transport, leading to a more confined footprint of concentration, higher overall concentration values, and a sharp gradient at the boundary of the jet, particularly visible in Fig. 13c–e.

The inability of the tested models to capture the correct turbulent transport near the wall is to be expected. In Fig. 11, angle misalignment was present in all three models along the bottom wall, particularly in the region of sharp concentration gradients in Fig. 13c–e. Disagreement of the wall-normal and spanwise components of the turbulent scalar flux vector are the greatest contributors to the angle misalignment metric. Misalignment of close to 90° along the bottom wall suggests that both wall-normal and spanwise components are being incorrectly modeled, leading to the failure to transport fluid from the jet down to the wall and then disperse it in the spanwise direction once it was there.

Angle misalignment is also high around the periphery of the jet hole exit and worsens with increasing model complexity. This can explain the higher concentrations predicted by the models around the edges of the jet hole exit. Increased turbulent mixing near the wall is also supported by Fig. 10c, which shows that Sc_t approaches 0 at the bottom wall, indicating that stronger turbulent mixing of the scalar occurs in this region compared to the rest of the jet. Additionally, in the analysis of the GGDH and HOGGDH performed by Abe and Suga,

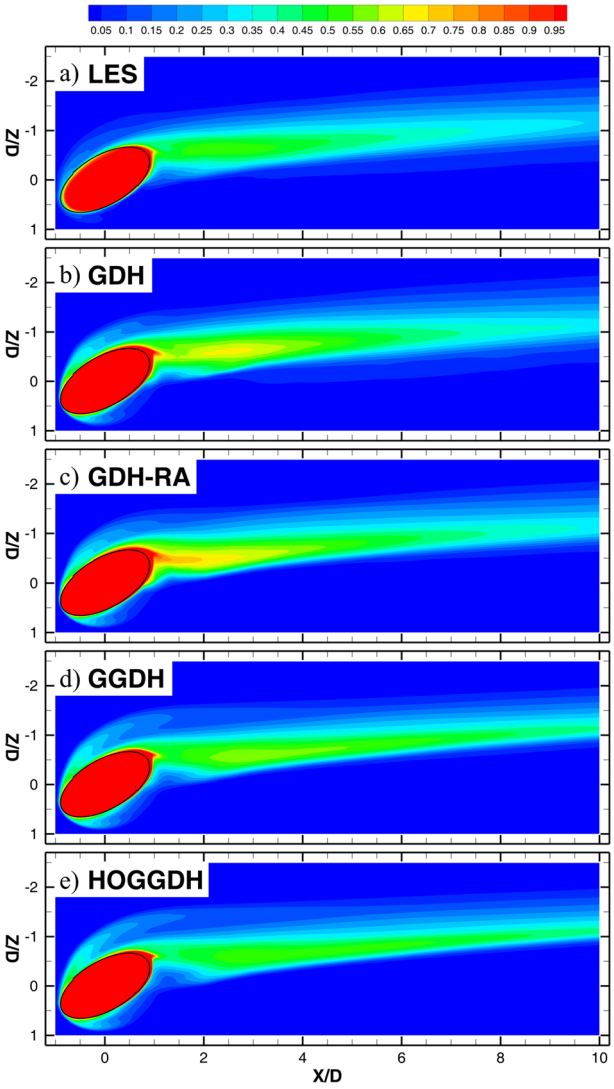

Fig. 13 Color contours of jet fluid concentration $\overline{C}$ at $Y = 0$ from (**a**) LES; (**b**) Case 1, isotropic α_t; (**c**) Case 3, $Sc_t = 0.35$; (**d**) Case 5, GGDH $\alpha_C = 0.45$; (**e**) Case 7, HOGGDH $\alpha_C = 0.5$

the value of the model constant α_C was found to increase by an order of magnitude when approaching the wall. The significant model errors in the near-wall region warrant further investigation and potentially special treatment in new models seeking to better capture the scalar transport in this region.

5 Conclusions

Mean velocity and concentration fields of a skewed jet in crossflow were measured using MRI-based techniques. The significant feature of the skewed jet is a single vortex which

governs development of the velocity and concentration fields by preferentially introducing slow, low-concentration fluid to one side of the jet. An LES of the same configuration, validated against the experiment, allowed for direct investigation of the turbulent scalar flux components in the jet region. The assumptions of isotropy and a uniform turbulent Schmidt number, commonly used in RANS calculations of this and other flows, were shown to be invalid for this jet in crossflow geometry. Three models typically used to represent the turbulent scalar fluxes, the GDH, GGDH, and HOGGDH, were evaluated based on their ability to capture scalar flux anisotropy. The GGDH and HOGGDH were found to better represent the scalar flux vector in large parts of the flow, although several areas remained unchanged or even slightly worsened with increasing model complexity. These models did improve the prediction of the concentration field over the isotropic values of the GDH-RA formulation. However, improvements related to switching to the GGDH and HOGGDH models relied on optimizing the model constant α_C. Using an optimized value instead of the default value suggested by the literature reduced model errors by up to 50 %. The improved concentration field predictions of the GGDH and HOGGDH over the GDH-RA show the importance of model anisotropy for the turbulence scalar fluxes; however, potentially equal improvements could be made using isotropic models which better capture the isotropic turbulent diffusivity extracted from the LES. Specifically, the optimized anisotropic models do not yet exceed the limit set by the optimal $\alpha_{t,iso}$ for isotropic models. Analysis showed that all models had difficulty predicting the amount of turbulence near the walls, particularly in underpredicting mixing downstream of injection.

Acknowledgments The authors gratefully acknowledge financial support from Honeywell Aerospace and ANSYS, Inc. J. B. and M. F. would like to thank continuous support and computational resources provided by CNRS on Turing (GENCI-IDRIS, Grant x20152a7178) and Eos (CALMIP, Grant 2015-p1425).

References

1. Aga, V., Abhari, R.S.: Influence of flow structure on compound angled film cooling effectiveness and heat transfer. J. Turbomach. **133**(3), 031,029 (2011)
2. Khan, Z.U., Johnston, J.P.: On vortex generating jets. Int. J. Heat Fluid Flow **21**(5), 506–511 (2000)
3. McGovern, K., Leylek, J.: A detailed analysis of film cooling physics: Part iicompound-angle injection with cylindrical holes. J. Turbomach. **122**(1), 113–121 (2000)
4. Johnson, P.L., Kapat, J.S.: Large-eddy simulations of a cylindrical film cooling hole. J. Thermophys. Heat Transfer **27**(2), 255–273 (2013)
5. Ziefle, J., Kleiser, L.: Assessment of a film-cooling flow structure by large-eddy simulation. J. Turb. **9**, N29 (2008)
6. Walters, D.K., Leylek, J.H.: A systematic computational methodology applied to a three-dimensional film-cooling flowfield. J. Turbomachinery **119**(4), 777–785 (1997)
7. Ivanova, E.M., Noll, B.E., Aigner, M.: A numerical study on the turbulent schmidt numbers in a jet in crossflow. J. Eng. Gas Turb. Power **135**(1), 011,505 (2013)
8. Daly, B.J., Harlow, F.H.: Transport equations in turbulence. Phys. Fluids **13**(11), 2634–2649 (1970)
9. Abe, K., Suga, K.: Towards the development of a Reynolds-averaged algebraic turbulent scalar-flux model. Int. J. Heat Fluid Flow **22**(1), 19–29 (2001)
10. Rossi, R., Iaccarino, G.: Numerical simulation of scalar dispersion downstream of a square obstacle using gradient-transport type models. Atmosph. Environ. **43**(16), 2518–2531 (2009)
11. Ling, J., Ryan, K.J., Bodart, J., Eaton, J.K.: Analysis of turbulent scalar flux models for a discrete hole film cooling flow. J. Turbomach. **138**(1), 011,006 (2016)
12. Li, X., Qin, Y., Ren, J., Jiang, H.: Algebraic anisotropic turbulence modeling of compound angled film cooling validated by particle image velocimetry and pressure sensitive paint measurements. J. Heat Transfer **136**(3), 032,201 (2014)
13. Azzi, A., Lakehal, D.: Perspectives in modeling film cooling of turbine blades by transcending conventional two-equation turbulence models. J. Turbomach. **124**(3), 472–484 (2002)

14. Pelc, N., Sommer, F., Li, K., Brosnan, T., Herfkens, R., Enzmann, D.: Quantitative magnetic resonance flow imaging. Magn. Resonan. Quart. **10**(3), 125–147 (1994)
15. Benson, M.J., Elkins, C.J., Mobley, P.D., Alley, M.T., Eaton, J.K.: Three-dimensional concentration field measurements in a mixing layer using magnetic resonance imaging. Exper. Fluids **49**(1), 43–55 (2010)
16. Bodart, J., Coletti, F., Bermejo-Moreno, I., Eaton, J.K.: High-fidelity simulation of a turbulent inclined jet in a crossflow. Center for Turbulence Research annual research brief, Stanford University, Stanford, CA (2013)
17. Vreman, A.: An eddy-viscosity subgrid-scale model for turbulent shear flow: Algebraic theory and applications. Phys. Fluids **16**(10), 3670–3681 (2004)